Electronic structure and resonant inelastic x-ray scattering in $Ca_3Ru_2O_7$

V. N. Antonov,[1,2] D. A. Kukusta,[1] and L. V. Bekenov[1]
[1]*G. V. Kurdyumov Institute for Metal Physics of the N.A.S. of Ukraine, UA-03142 Kyiv, Ukraine*
[2]*Max Planck Institute for Solid State Research, 70569 Stuttgart, Germany*

(Received 25 April 2024; accepted 14 June 2024; published 1 July 2024)

We have investigated the electronic structure of the transition metal oxide $Ca_3Ru_2O_7$ within density-functional theory using the generalized gradient approximation while considering strong Coulomb correlations in the framework of the fully relativistic spin-polarized Dirac linear muffin-tin orbital band structure method. $Ca_3Ru_2O_7$ can be classified as a Mott insulator since it was expected to be metallic from band structure calculations. We found that the magnetic ground state of $Ca_3Ru_2O_7$ possesses an AFM-b magnetic structure with the Ru spin moments ordered antiferromagnetically along the b axis. We have investigated the resonant inelastic x-ray scattering (RIXS) spectra at the Ru and Ca K, L_3, and M_3 edges as well as at the O K edge. The experimentally measured RIXS spectrum of $Ca_3Ru_2O_7$ at the Ru L_3 edge possesses a sharp feature $\leqslant$2 eV corresponding to transitions within the Ru t_{2g} levels. The excitation located from 2 to 4 eV is due to $t_{2g} \rightarrow e_g$ transitions. The third wide structure situated at $4.5 - 11$ eV appears due to transitions between the Ru $4d_{\mathrm{O}}$ states derived from the tails of oxygen $2p$ states and e_g and t_{2g} states. The RIXS spectra at the Ru L_3 and M_3 edges are quite similar. However, the corresponding RIXS spectra at the Ca site are quite different from each other due to the significant difference in the widths of core levels. The RIXS spectrum at the O K edge consists of three major inelastic excitations. We found that the first two low energy features $\leqslant$2.5 eV are due to interband transitions between occupied and empty $O_{t_{2g}}$ states which appear due to the strong hybridization between oxygen $2p$ and Ru t_{2g} states in close vicinity to the Fermi level. The next major peak between 2.5 and 8 eV reflects interband transitions from occupied O $2p$ to empty $O_{t_{2g}}$ states. A wide energy interval between 4 and 11 eV is occupied by rather weak $O_{2p} \rightarrow O_{e_g}$ transitions.

DOI: 10.1103/PhysRevMaterials.8.074401

I. INTRODUCTION

Ruddlesden-Popper (RP)-type ruthenates $A_{n+1}Ru_nO_{3n+1}$ (A = Sr or Ca), where n is a number of Ru-O layers per unit cell, have attracted much attention due to their fascinated physical properties. For example, Sr_2RuO_4 ($n = 1$) possesses a unique p-wave superconductivity [1,2]; however, Ca_2RuO_4 is a typical Mott insulator [3]. In the $n = \infty$ family, $SrRuO_3$ is a ferromagnetic metal [3], whereas $CaRuO_3$ does not show any magnetic ordering [4]. Double-layered $Sr_3Ru_2O_7$ ($n = 2$) has an orthorhombic crystal structure (space group *Bbcb*, No. 68) [5], where RuO_6 octahedra rotate around the c axis. The ionic radius of Ca^{2+} is smaller than that of Sr^{2+}; therefore, $Ca_3Ru_2O_7$ has a more distorted crystal structure, namely the orthorhombic symmetry with $Bb2_1m$ space group (No. 36) with rotation and tilting of RuO_6 octahedra [6,7]. $Sr_3Ru_2O_7$ is a metal with unusual large quasiparticle masses [8], it shows the Fermi-liquid behavior, and ferromagnetic instability in the ground state [9]. However, $Ca_3Ru_2O_7$ is a Mott-like antiferromagnetic (AFM) insulator, where ferromagnetic bilayers stack antiparallel along the c axis (Néel temperature $T_N = 56$ K) [10,11]. This ruthenate possesses the first-order metal-to-insulator transition at $T_{MI} = 48$ K that distorts the RuO_6 octahedra and coincides with an upturn in the out-of-plane resistivity [7,12]. A spin rotation from the a axis to the b axis (AFM-b) occurs at T_{MI} that appears to be mediated by an incommensurate spin state [13,14]. The system also shows complex magnetic field dependence [15,16]. $Ca_3Ru_2O_7$ stimulated much research effort due to its colossal magnetoresistance and anisotropic magnetic behavior [10,12,17–19]. This bilayer compound also retains highly anisotropic electric resistivity down to the lowest temperatures [13]. Specific-heat and photoemission studies [20,21] indicate unusual behavior for the density of states (DOS) and bandwidth of $Ca_3Ru_2O_7$ at low temperatures, reflecting strong electron correlation effects in the $4d$ band. The optical conductivity shows a small energy gap of 25 meV at low temperature [22]. The Raman spectra measurements by Liu *et al.* [23] reveal a charge energy gap of $\Delta_c \sim 96$ meV in $Ca_3Ru_2O_7$. The large gap ratio $\Delta_c/k_BT_{MI} = 23$ associated with this gap is indicative of strong electronic correlations, perhaps pointing to a Mott-Hubbard-type transition. It is believed that the wide spread of physical phenomena in these ruthenates is due to a delicate balance of competing interactions, such as orbital degrees of freedom, crystal structure distortion, electron correlation, and spin-orbit coupling (SOC) [24–29].

There are several band structure calculations of $Ca_3Ru_2O_7$ based on the density-functional theory (DFT) [30–34]. Singh and Auluck provided the band structure calculations of $Ca_3Ru_2O_7$ and found that the local spin-density approximation (LSDA) failed to reproduce the insulating ground state [30]. Liu reported an electronic structure study on $Ca_3Ru_2O_7$ using first-principles calculations including the SOC and on-site Coulomb interaction [31]. He found that the observed insulating ground state of $Ca_3Ru_2O_7$ can be reproduced if the magnetic moments are aligned along the b axis.

In the present study, we focus on the electronic structure and resonant inelastic x-ray scattering (RIXS) spectra of $Ca_3Ru_2O_7$. The RIXS measurements at the Ru L_3 edge for the $Ca_3Ru_2O_7$ ruthenate have been successfully performed recently by Bertinshaw *et al.* [29]. They capture the in-plane magnon across the entire Brillouin zone, giving a spin-wave gap of ∼8 meV. At a higher energy loss, they observe dd-type excitations between the t_{2g} and e_g bands. The measurements of the oxygen K RIXS spectrum are provided in Ref. [35]. The authors resolve two intra-t_{2g} excitations in $Ca_3Ru_2O_7$. The lowest lying excitation is interpreted as a magnetic transverse mode with multiparticle character. They also observe a quite intensive peak at ∼3.3 eV in the O K RIXS spectrum.

In this article, we report a detailed theoretical DFT study of the electronic structure and RIXS spectra of the $Ca_3Ru_2O_7$ oxide at the Ru and Ca K, L_3, and M_3 edges as well as at the O K edge to investigate the influence of the SOC and Coulomb correlations. The energy band structure of this RP ruthenate was calculated using the fully relativistic spin-polarized Dirac linear muffin-tin orbital (LMTO) band structure method. We used both the generalized gradient approximation (GGA) and the GGA + U approach to assess the sensitivity of the RIXS results to different treatment of the correlated electrons.

This article is organized as follows. The crystal structures of $Ca_3Ru_2O_7$ and computational details are presented in Sec. II. Section III presents the electronic and magnetic structures of this ruthenate. In Sec. IV, the theoretical investigations of the RIXS spectra of $Ca_3Ru_2O_7$ at the Ru and Ca K, L_3 edges and at the O K edge are presented. The theoretical results are compared with available experimental data. Finally, the results are summarized in Sec. V.

II. COMPUTATIONAL DETAILS

A. Resonant inelastic x-ray scattering

In the direct RIXS process [36], the incoming photon with energy $\hbar\omega_{\mathbf{k}}$, momentum $\hbar\mathbf{k}$, and polarization $\boldsymbol{\epsilon}$ excites the solid from the ground state $|\mathrm{g}\rangle$ with energy E_g to the intermediate state $|\mathrm{I}\rangle$ with energy E_I. During relaxation, an outgoing photon with energy $\hbar\omega_{\mathbf{k}'}$, momentum $\hbar\mathbf{k}'$, and polarization $\boldsymbol{\epsilon}'$ is emitted, and the solid is in state $|f\rangle$ with energy E_f. As a result, an excitation with energy $\hbar\omega = \hbar\omega_{\mathbf{k}} - \hbar\omega_{\mathbf{k}'}$ and momentum $\hbar\mathbf{q} = \hbar\mathbf{k} - \hbar\mathbf{k}'$ is created. Our implementation of the code for the calculation of the RIXS intensity uses Dirac four-component basis functions [37] in the perturbative approach [38]. RIXS is the second-order process, and its intensity is given by

$$I(\omega, \mathbf{k}, \mathbf{k}', \boldsymbol{\epsilon}, \boldsymbol{\epsilon}') \propto \sum_{\mathrm{f}} \left| \sum_{\mathrm{I}} \frac{\langle \mathrm{f}|\hat{H}'_{\mathbf{k}'\boldsymbol{\epsilon}'}|\mathrm{I}\rangle\langle \mathrm{I}|\hat{H}'_{\mathbf{k}\boldsymbol{\epsilon}}|\mathrm{g}\rangle}{E_\mathrm{g} - E_\mathrm{I}} \right|^2 \times \delta(E_\mathrm{f} - E_\mathrm{g} - \hbar\omega), \quad (1)$$

where the RIXS perturbation operator in the dipole approximation is given by the lattice sum $\hat{H}'_{\mathbf{k}\boldsymbol{\epsilon}} = \sum_{\mathbf{R}} \hat{\boldsymbol{\alpha}}\boldsymbol{\epsilon} \exp(-\mathrm{i}\mathbf{k}\mathbf{R})$, where α are the Dirac matrices. The sum over the intermediate states $|\mathrm{I}\rangle$ includes the contributions from different spin-split core states at the given absorption edge. The matrix elements of the RIXS process in the frame of the fully relativistic Dirac LMTO method were presented in our previous publication [39].

B. X-ray magnetic circular dichroism

Magneto-optical (MO) effects refer to various changes in the polarization state of light upon interaction with materials possessing a net magnetic moment, including rotation of the plane of linearly polarized light (Faraday, Kerr rotation), and the complementary differential absorption of left and right circularly polarized light (circular dichroism). In the near visible spectral range, these effects result from excitation of electrons in the conduction band. Near x-ray absorption edges, or resonances, MO effects can be enhanced by transitions from well-defined atomic core levels to transition symmetry selected valence states.

Within the one-particle approximation, the absorption coefficient $\mu_j^\lambda(\omega)$ for incident x-ray polarization λ and photon energy $\hbar\omega$ can be determined as the probability of electronic transitions from initial core states with the total angular momentum j to final unoccupied Bloch states

$$\mu_j^\lambda(\omega) = \sum_{m_j} \sum_{n\mathbf{k}} |\langle \Psi_{n\mathbf{k}}|\Pi_\lambda|\Psi_{jm_j}\rangle|^2 \delta(E_{n\mathbf{k}} - E_{jm_j} - \hbar\omega) \times \theta(E_{n\mathbf{k}} - E_F), \quad (2)$$

where Ψ_{jm_j} and E_{jm_j} are the wave function and the energy of a core state with the projection of the total angular momentum m_j, $\Psi_{n\mathbf{k}}$ and $E_{n\mathbf{k}}$ are the wave function and the energy of a valence state in the n-th band with the wave vector $\mathbf{k}$, and E_F is the Fermi energy.

Here, Π_λ is the electron-photon interaction operator in the dipole approximation

$$\Pi_\lambda = -e\boldsymbol{\alpha}\mathbf{a}_\lambda, \quad (3)$$

where $\boldsymbol{\alpha}$ are the Dirac matrices and $\mathbf{a}_\lambda$ is the λ polarization unit vector of the photon vector potential, with $a_\pm = 1/\sqrt{2}(1, \pm i, 0)$, $a_\parallel = (0, 0, 1)$. Here, + and − denote, respectively, left and right circular photon polarizations with respect to the magnetization direction in the solid. Then, x-ray magnetic circular and linear dichroisms are given by $\mu_+ - \mu_-$ and $\mu_\parallel - (\mu_+ + \mu_-)/2$, respectively. More detailed expressions of the matrix elements in the electric dipole approximation may be found in Refs. [40–42]. The matrix elements due to magnetic dipole and electric quadrupole corrections are presented in Ref. [42].

TABLE I. The atomic as well as Wyckoff positions (WP) of $Ca_3Ru_2O_7$ with $Bb2_1/m$ lattice symmetry (lattice constants $a = 5.3677$ Å, $b = 5.5356$ Å, and $c = 19.5212$ Å) at temperature of 8 K [7].

Atom	WP	x	y	z
Ca_1	4a	0.7382	0.1949	0
Ca_2	8b	0.2443	0.3036	0.3112
Ru	8b	0.2533	0.7512	0.4011
O_1	8b	0.8188	0.2309	0.6987
O_2	4a	0.3370	0.7702	0.5
O_3	8b	0.4474	0.9500	0.0819
O_4	8b	0.9481	0.0458	0.1162

C. Crystal structure

$Ca_3Ru_2O_7$ has the orthorhombic symmetry with $Bb2_1m$ space group (No. 36) with the rotation and tilting of RuO_6 octahedra [6,7] (Table I and Fig. 1). The structure of $Ca_3Ru_2O_7$ consists of an RuO_6 double layer and CaO layer per unit cell. The Ru^{4+} cations are surrounded by oxygen octahedra with the interatomic distances Ru-O_1, Ru-O_2, Ru-O_3, and Ru-O_4 of 1.9872, 1.9873, 2.0033, and 1.9949 Å, respectively. The inter-atomic distances between Ru and Ca_1 and Ca_2 ions are equal to 3.1263 and 3.0355 Å, respectively.

The neutron diffraction measurements show that the lattice constants a and c of $Ca_3Ru_2O_7$ shorten on cooling from room temperature, whereas b elongates [7]. At the first-order transition temperature of 48 K, the lattice parameters jump; however, the space group symmetry $Bb2_1m$ is not affected throughout the temperature range measured [7]. The c constant shortens by about 0.1%, whereas both a and b lengthen by about 0.07% at T_{MI}.

The lengths of Ru-O_1 and Ru-O_3 bonds increase with decreasing temperature. Yet, those of Ru-O_2 and Ru-O_4 decrease with decreasing temperature. The angles between the RuO_6 octahedra are almost temperature independent above T_N and little affected by the first-order phase transition. However, some characteristic temperature dependences can be observed $\leqslant$40 K [7]. The angle of Ru-O_1-Ca_2 decreases with decreasing temperature. Yet, the angle of Ru-O_2-Ru increases with decreasing temperature [7].

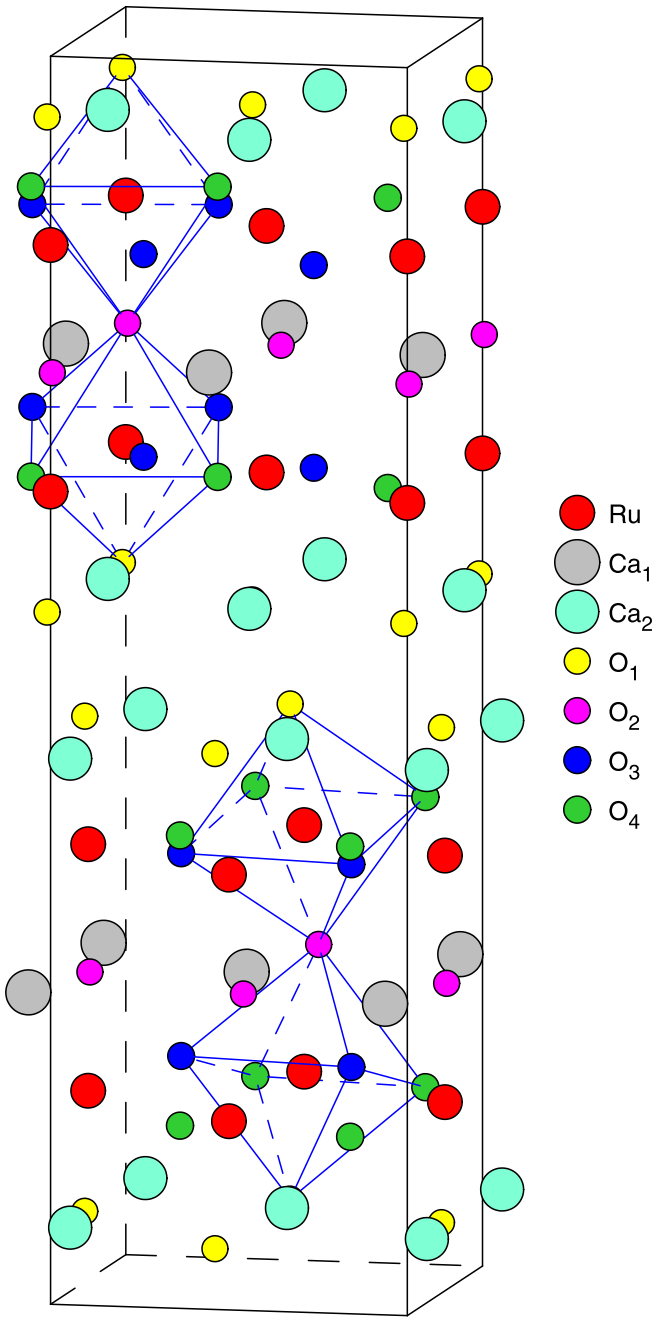

FIG. 1. The crystal structure of $Ca_3Ru_2O_7$ (space group $Bb2_1m$, No. 36) [7] with Ru^{3+} ions in octahedral oxygen coordination.

D. Calculation details

The details of the computational method are described in our previous works [39,43–45], and here we only mention several aspects. The band structure calculations were performed using the fully relativistic LMTO method [41,46]. This implementation of the LMTO method uses four-component basis functions constructed by solving the Dirac equation inside an atomic sphere [37]. The exchange-correlation functional of the GGA type was used in the version of Perdew *et al.* [47]. Brillouin zone integration was performed using the improved tetrahedron method [48]. The basis consisted of Ca and Ru s, p, d, and f, and O s, p, and d LMTOs.

To consider the electron-electron correlation effects, in this work we use the relativistic generalization of the rotationally invariant version of the GGA + U method [49] which takes into account that, in the presence of SOC, the occupation matrix of localized electrons becomes nondiagonal in spin indexes. Hubbard U was considered an external parameter and varied from 0.8 to 3.8 eV for the 4d Ru site. The values of exchange Hund coupling used in our calculations were obtained from constrained LSDA calculations [50,51] and equal to $J_H = 0.8$ eV for Ru. Thus, the parameter $U_{eff} = U - J_H$, which roughly determines the splitting between the lower and upper Hubbard bands, varied between 0 and 3.0 eV for the 4d metal site. We adjusted the value of U to achieve the best agreement with the experiment.

X-ray absorption spectroscopy (XAS), x-ray magnetic circular dichroism (XMCD), and RIXS spectra were calculated

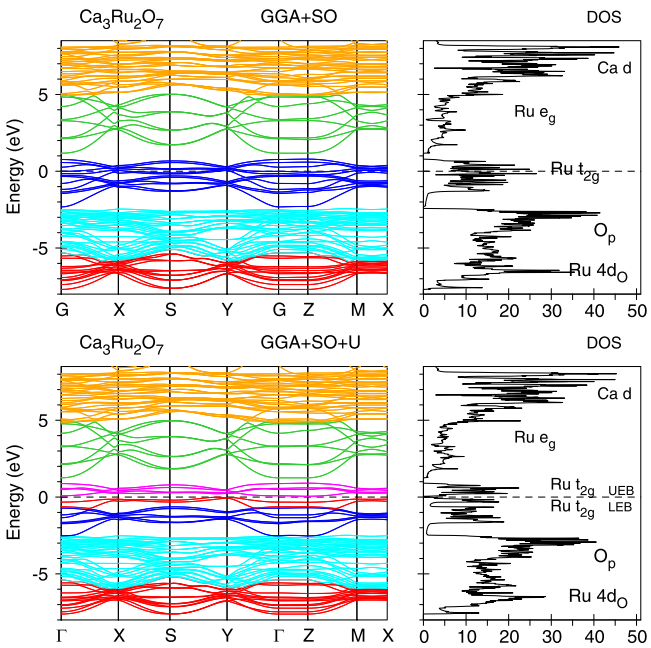

FIG. 2. The energy band structure and total DOS [in states/(cell eV)] of $Ca_3Ru_2O_7$ calculated in the GGA + SO approximation (the upper panel) and GGA + SO + U approach (the lower panel).

taking into account the exchange splitting of core levels. The finite lifetime of a core hole was accounted for by folding the spectra with a Lorentzian. The widths of core levels Γ for Ca, Ru, and O were taken from Ref. [52]. The finite experimental resolution of the spectrometer was accounted for by a Gaussian of 0.6 eV (the s coefficient of the Gaussian function).

III. ELECTRONIC AND MAGNETIC STRUCTURES

Figure 2 presents the energy band structure of $Ca_3Ru_2O_7$ calculated in the fully relativistic Dirac GGA + SO approximation (the upper panel) and considering Coulomb correlations in the GGA + SO + U approach (the lower panel). The GGA + SO approximation produces a metallic ground state in $Ca_3Ru_2O_7$ in contradiction to the experimental data which show that $Ca_3Ru_2O_7$ is a Mott-like AFM insulator below $T_{MI} = 48$ K [7,10–12]. To produce the correct ground state, one has to take into account strong Coulomb correlations in $Ca_3Ru_2O_7$. The GGA + SO + U approach shifts the occupied and empty t_{2g} bands downward and upward, respectively, by $U_{eff}/2$ producing a direct energy gap of 0.215 eV and an indirect one of 0.053 eV for $U_{eff} = 1.3$ eV. We found that this value of Hubbard U applied for the Ru site produces the best agreement between the calculated and experimentally measured RIXS spectra at the Ru L_3 edge in $Ca_3Ru_2O_7$. The energy gap is increased with increasing Hubbard U.

Figure 3 presents the partial DOS in $Ca_3Ru_2O_7$ calculated in the GGA + SO + U approach. Four electrons occupy the t_{2g}-type low energy band (LEB) manifold in the energy interval from −1.7 to −0.6 eV and between −0.35 eV and E_F in $Ca_3Ru_2O_7$ (blue and red curves in the lower panel of Fig. 2, respectively). The empty t_{2g} states [the upper energy band (UEB)] occupy the energy range from 0.1 to 0.9 eV (magenta

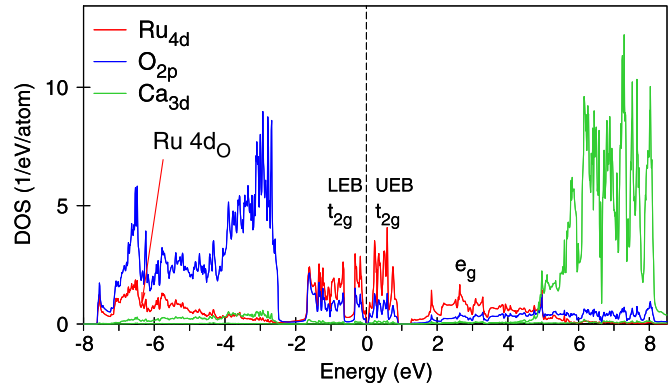

FIG. 3. The partial DOS in $Ca_3Ru_2O_7$ calculated in the GGA + SO + U approach with $U_{eff} = 1.3$ eV.

curves in the lower panel of Fig. 2). The symmetry analysis shows that the empty t_{2g} states just above the Fermi level possess the combination of d_{xz} and d_{yz} orbitals. The e_g-type states of Ru are distributed far above the Fermi level from 1.3 to 5.0 eV (green bands in Fig. 2). The occupation number of 4d electrons in the Ru atomic sphere is equal to 5.66, which is much larger than the expected value of four t_{2g} electrons in Ru^{4+}. The excessive charge is provided by the tails of O 2p states inside the Ru atomic spheres. These charge transfer $4d_O$ states, which are located from −7.6 to approximately −5.0 eV (red bands in Fig. 2), play an essential role for the RIXS spectrum at the Ru $L_{2,3}$ edges (see Sec. IV). The Ca 3d states are mostly empty and located from 5.0 to 8.2 eV above the Fermi level (yellow bands in Fig. 2). The oxygen 2p states are strongly hybridized with the Ru 4d states due to small interatomic O-Ru distances and delocalized nature of O 2p states. They occupy the energy interval between −7.6 and −2.5 eV (light blue bands in Fig. 2). The small peaks in the vicinity of the Fermi level are due to the hybridization between O 2p and Ru t_{2g} LEB and UEB.

We found that in the ground state, $Ca_3Ru_2O_7$ possesses an AFM-b magnetic structure with the Ru spin moments ordered antiferromagnetically along the b axis (Fig. 4). This is consistent with experimental data [13,14] and previous band structure calculations [31].

Table II presents the theoretically calculated spin M_s, orbital M_l, and total M_{tot} magnetic moments in $Ca_3Ru_2O_7$. The Ru spin and orbital moments are parallel in $Ca_3Ru_2O_7$ in accordance with Hund's third rule. The spin and orbital parts of the magnetic moments for the Ca ions in $Ca_3Ru_2O_7$ are found to be quite small. The spin and orbital magnetic moments at the oxygen sites are also relatively small with the largest moments at the O_4 site and the smallest ones at the O_2 site.

IV. XAS, XMCD, AND RIXS SPECTRA

A. Ru L_3 and M_3 XAS, XMCD, and RIXS spectra

The experimental RIXS spectrum at the Ru L_3 edge was measured by Bertinshaw *et al.* [29] in the energy range up to 6.5 eV. In addition to an elastic peak centered close to zero energy loss, the spectrum consists of a peak at ∼0.5 eV with a high energy shoulder at 1.3 eV and two peaks at 3

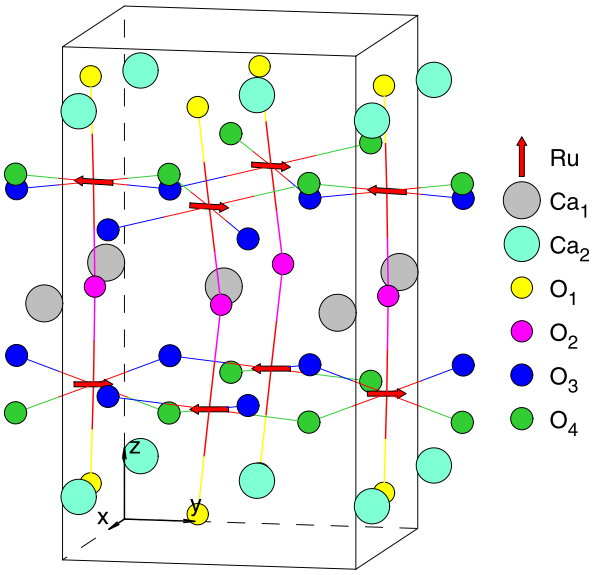

FIG. 4. Half of the $Ca_3Ru_2O_7$ unit cell with AFM-ordered Ru moments parallel to the b axis (the AFM-b order).

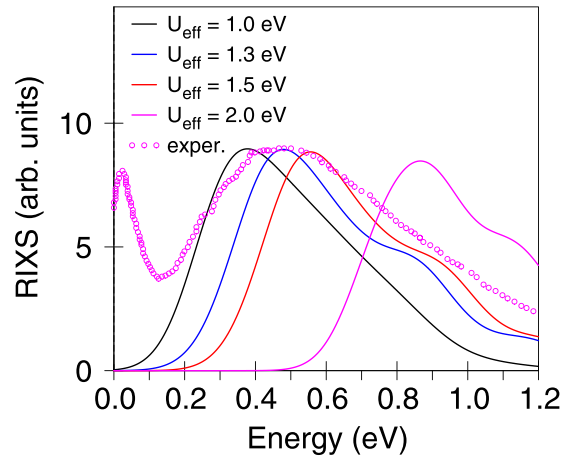

FIG. 5. The experimental RIXS spectrum measured at 25 K by Bertinshaw *et al.* [29] (open magenta circles) at the Ru L_3 edge of $Ca_3Ru_2O_7$ compared with the theoretical spectra calculated for $t_{2g} \rightarrow t_{2g}$ transitions with different U_{eff}.

and 5.8 eV. We found that the two peak structure situated $\leqslant$2 eV corresponds to intra-t_{2g} excitations. These peaks are quite sensitive to the value of the energy gap in $Ca_3Ru_2O_7$ and the relative position of the t_{2g} LEB and UEB (see Fig. 2). Figure 5 shows the experimental RIXS spectrum measured by Bertinshaw *et al.* [29] (open magenta circles) in comparison with the theoretical spectra calculated for $t_{2g} \rightarrow t_{2g}$ transitions with different values of U_{eff}. The best agreement was found for the GGA + SO + U approach with $U_{eff} = 1.3$ eV. The calculations with larger U_{eff} shift the RIXS spectrum toward higher energies.

From Fig. 5, we can see that there is an additional peak at 0.05 eV with a width of ~30 meV in the experimentally measured Ru L_3 RIXS spectrum which is not reproduced by our one-partial calculations. Bertinshaw *et al.* [29] show that this peak corresponds to a magnon excitation at the zone center, in agreement with inelastic neutron scattering data. The magnon dispersion was theoretically modeled using a Heisenberg Hamiltonian for a bilayer $S = 1$ system with single-ion anisotropy terms [29]. In addition to the 0.05 eV peak, other low energy peaks at 0.2–0.4 eV, which look like shoulder peaks, are also missing within our theoretical model. We can suggest that these small shoulders at 0.2–0.4 eV can be attributed to exciton spectra. A similar situation was observed in Sr_2IrO_4 at the Ir L_3 edge where detected extra peaks at 0.1 and 0.4 eV were attributed to magnon and exciton excitations, respectively [53–56]. The theoretical description of magnon and exciton spectra demands a many-body approach beyond one-particle approximation, such as GW or BSE (Bethe-Salpeter equation) calculations for the exciton spectra and calculations of magnon dispersion and electron-magnon interaction for the magnon spectra. An approach which allows for a unified description of both magnon and exciton excitations on the same footing and taking into account the RIXS matrix elements is highly desirable.

TABLE II. The theoretically calculated in GGA+SO+U ($U_{eff} = 1.3$ eV) spin M_s, orbital M_l, and total M_{tot} magnetic moments (in μ_B) in $Ca_3Ru_2O_7$.

Atom	M_s	M_l	M_{total}
Ca_1	0.0002	0.0007	0.0009
Ca_2	0.0165	0.0014	0.0179
Ru	1.4783	0.1370	1.6153
O_1	0.0625	0.0072	0.0697
O_2	0.0120	−0.0065	0.0055
O_3	0.1008	0.0097	0.1105
O_4	0.1141	0.0096	0.1237

Figure 6 (the lower panel) presents the experimental RIXS spectrum (open magenta circles) at the Ru L_3 edges for $Ca_3Ru_2O_7$ [29] in a wide energy interval in comparison with the theoretically calculated partial contributions from different interband transitions in the GGA + SO + U approach. As mentioned previously, the two peaks situated $\leqslant$2 eV correspond to intra-t_{2g} excitations (dashed and dotted blue curves in Fig. 6). We divided the occupied part of the t_{2g} energy band into two groups—4 bands in close vicinity to the Fermi level (blue curves in Fig. 2) and the other 12 bands situated at lower energy (red curves in Fig. 2)—and calculated the interband transitions from these two groups to empty t_{2g} states (magenta curves in Fig. 2) separately. We found that the small number of occupied bands in close vicinity to the Fermi level produce a larger RIXS signal (peak α) than the large number of LEBs (peak β) due to corresponding matrix elements. The peak γ located at ~3 eV (red curve in the lower panel of Fig. 6) was found to be due to $t_{2g} \rightarrow e_g$ transitions. The strong fine structure δ at ~5.8 eV (green curve) is due to $4d_O \rightarrow t_{2g}$ transitions. The structure which extends from 7 up to 11 eV (the magenta curve) presents $4d_O \rightarrow e_g$ transitions. The theoretical calculations are in good agreement with the experimental data.

Figure 6 (the upper panel) shows the theoretically calculated RIXS spectrum at the Ru M_3 edge presented as partial

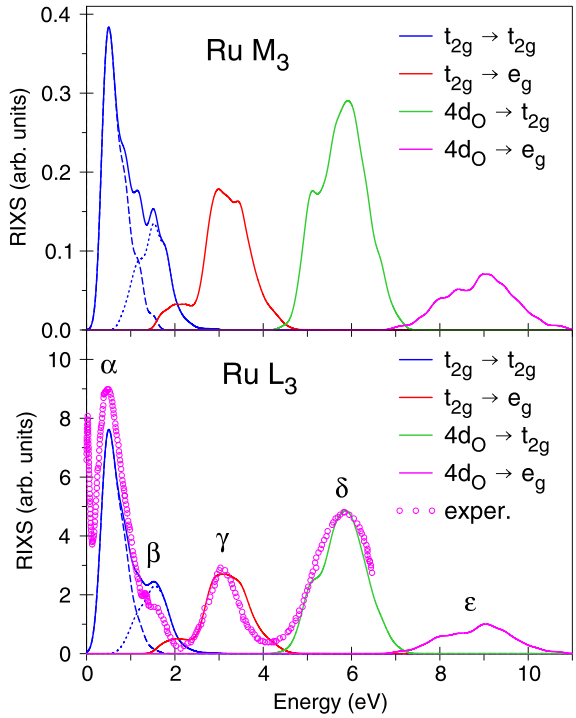

FIG. 6. The experimental RIXS spectrum (open magenta circles) measured at 25 K by Bertinshaw *et al.* [29] at the Ru L_3 edge of $Ca_3Ru_2O_7$ compared with the theoretically calculated partial contributions to the RIXS spectrum from different interband transitions (the lower panel). The upper panel presents the theoretically calculated partial contributions to the RIXS spectrum from different interband transitions at the M_3 edge. The calculations were carried out in the GGA + SO + U approach with $U_{eff} = 1.3$ eV.

contributions from different interband transitions. The shape of the spectrum is quite similar to the corresponding spectrum at the Ru L_3 edge, but with approximately 1 order of magnitude smaller intensity.

Figure 7 shows the theoretically calculated XAS (the upper panel) and XMCD (the lower panel) spectra at the Ru L_3 and M_3 edges of $Ca_3Ru_2O_7$ calculated in the GGA + SO + U approach. The widths of the $2p_{3/2}$ and $3p_{3/2}$ core levels are close ($\Gamma_{2p_{3/2}} = 1.87$ eV and $\Gamma_{3p_{3/2}} = 2.2$ eV [52]). Therefore, both the Ru L_3 and M_3 XAS spectra possess quite similar structures with a major peak at ∼3 eV, a low energy shoulder at 0.7 eV, and an additional high energy peak at 15 eV. The last fine structure is due to the hybridization of Ru $4d$ states with the oxygen $2p$ states which have a corresponding peak at 15 eV above the Fermi level (not shown). Two low energy fine structures in the Ru L_3 (M_3) XAS spectrum $\leqslant 5$ eV are due to transitions from the core $2p_{3/2}$ ($3p_{3/2}$) level to empty t_{2g} (the low energy shoulder) and e_g (the major peak) states. The transitions to e_g states have larger intensity in comparison with the corresponding transitions into empty t_{2g} states. The XMCD spectra also have a two-peak structure (lower panel of Fig. 7), but these spectra are dominated by transitions into empty t_{2g} states with a small contribution from empty e_g orbitals at higher energy. The XMCD spectrum at the M_3 edge is much smaller than at the L_3 edge.

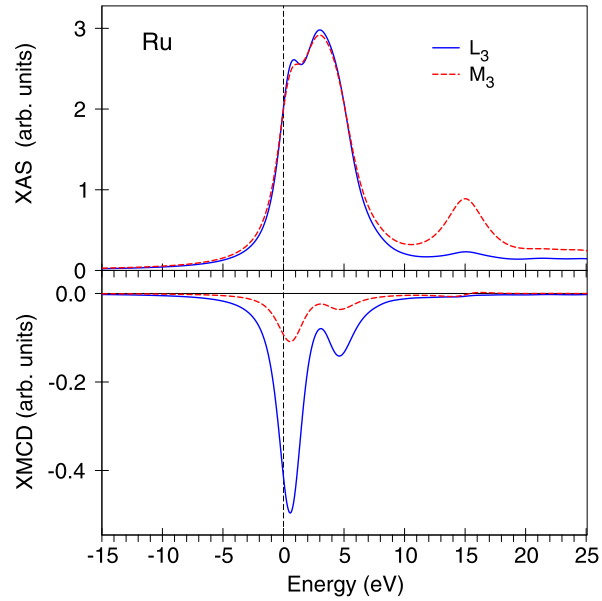

FIG. 7. The theoretically calculated XAS (the upper panel) and XMCD (the lower panel) spectra at the Ru L_3 and M_3 edges of $Ca_3Ru_2O_7$ calculated in the GGA + SO + U approach with $U_{eff} = 1.3$ eV.

B. Ca L_3 and M_3 XAS, XMCD, and RIXS spectra

Figure 8 shows the theoretically calculated XAS (the upper panel) and XMCD (the lower panel) spectra at the Ca L_3 and M_3 edges of $Ca_3Ru_2O_7$. The Ca $3d$ partial DOS is situated far above the Fermi level (see Fig. 3). Therefore, both the Ca L_3 and M_3 XAS spectra possess one-peak structures at ∼7 eV above the Fermi level. The Ca M_3 XAS spectrum is

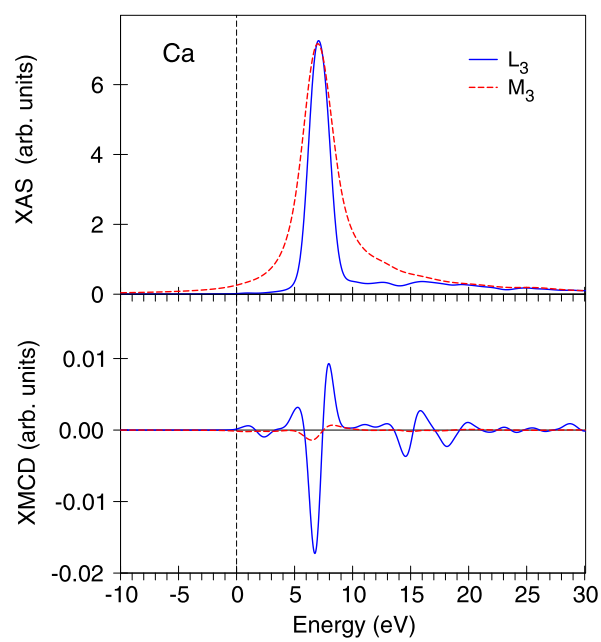

FIG. 8. The theoretically calculated XAS (the upper panel) and XMCD (the lower panel) spectra at the Ca L_3 and M_3 edges of $Ca_3Ru_2O_7$ calculated in the GGA + SO + U approach with $U_{eff} = 1.3$ eV.

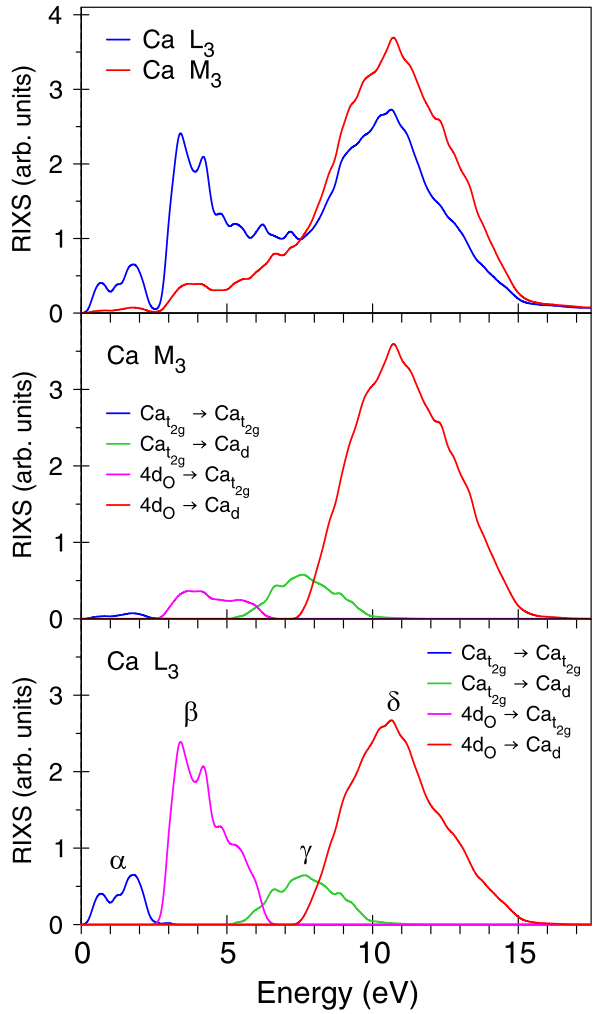

FIG. 9. The theoretically calculated RIXS spectra at the Ca L_3 and M_3 edges in $Ca_3Ru_2O_7$ (the upper panel) calculated in the GGA + SO + U approach ($U_{eff} = 1.3$ eV) and partial contributions to the RIXS spectra from different interband transitions at the Ca M_3 (the middle panel) and Ca L_3 edges (the lower panel).

much wider than the corresponding L_3 spectrum due to a significantly larger width of the $3p_{3/2}$ core level in comparison with the $2p_{3/2}$ one [52]. The Ca L_3 XMCD spectrum has a complicated shape with several positive and negative peaks. It is more than 1 order of magnitude smaller than the Ru L_3 XMCD spectrum (the lower panel of Fig. 7) due to smaller SOC, spin, and orbital magnetic moments at the Ca site in comparison with the Ru site (see Table II). The dichroism at the Ca M_3 edge is quite small even compared to the Ca L_3 XMCD spectrum.

Figure 9 show the theoretically calculated RIXS spectra at the Ca L_3 and M_3 edges in $Ca_3Ru_2O_7$ (the upper panel) and partial contributions to the RIXS spectra from different interband transitions at the Ca M_3 (the middle panel) and Ca L_3 edges (the lower panel). The low energy two-peak fine structure $\alpha \leqslant 2.5$ eV (blue curve) was found to be due to $Ca_{t_{2g}} \rightarrow Ca_{t_{2g}}$ transitions, or more precisely, between Ca $3d$ occupied and empty states, which are located in the energy region of Ru t_{2g} states from -1.7 eV to E_F and from 0.1 to

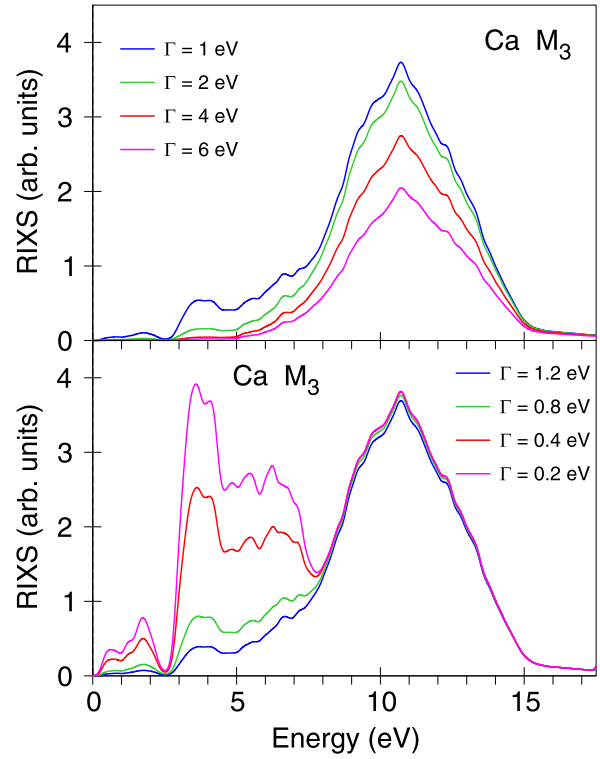

FIG. 10. The theoretically calculated RIXS spectra at the Ca M_3 edge in $Ca_3Ru_2O_7$ obtained for different parameters Γ.

0.9 eV, respectively (see Fig. 3). The next fine structure β located between 2.5 and 6.5 eV arises from interband transitions between $4d_O$ states (which are derived from the tails of oxygen $2p$ states inside the Ca atomic spheres) and $Ca_{t_{2g}}$ states. The peak γ is due to interband transitions from $Ca_{t_{2g}}$ states to the Ca empty $4d$ states. The large high energy peak δ is due to $4d_O \rightarrow Ca_d$ transitions.

The RIXS spectra at the L_3 and M_3 edges have to possess similar shapes because they reflect interband transitions between $d_{5/2}$ band states and the $2p_{3/2}$ and $3p_{3/2}$ core levels, respectively. This is true indeed in the case of the Ru L_3 and M_3 RIXS spectra (see Fig. 6). However, the L_3 and M_3 RIXS spectra at the Ca site differ from each other (the upper panel of Fig. 9). There is strong suppression of the low energy peaks α and β in the Ca M_3 RIXS spectrum in comparison with the Ca L_3 spectrum. Such a puzzle can be explained by the significant difference in the widths of corresponding core levels ($\Gamma_{3p_{3/2}} = 1.2$ eV and $\Gamma_{2p_{3/2}} = 0.21$ eV [52]). Figure 10 shows the theoretically calculated RIXS spectra at the Ca M_3 edge in $Ca_3Ru_2O_7$ obtained for different core-level parameters Γ. Under decreasing the parameter Γ from 1.2 to 0.2 eV, the intensity of the low energy peaks α and β is increased and the shape of the Ca M_3 RIXS spectrum is transformed to the L_3 one. The high energy peak δ does not change its shape. However, when we changed the parameter Γ to a greater extent from 1 to 6 eV, we found that the intensity of the peak δ monotonously decreased.

It should be mentioned that the x-ray absorption and RIXS processes have different nature. The matrix elements of the RIXS process are more complicated than the x-ray absorption ones [38,39,41]. As a result, the XAS spectra possess linear

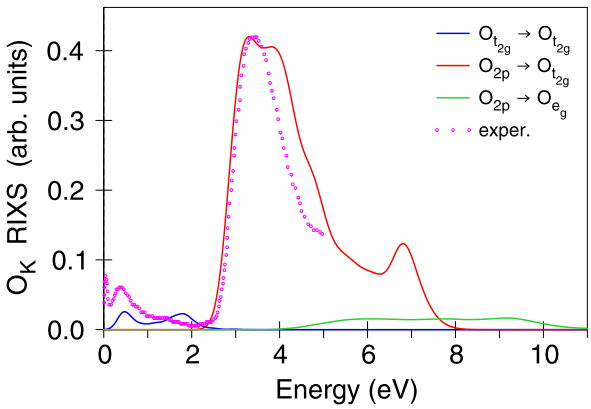

FIG. 11. The theoretically calculated RIXS spectrum at the O K edge in $Ca_3Ru_2O_7$ obtained in the GGA + SO + U approach ($U_{eff} = 1.3$ eV) and partial contributions to the RIXS spectrum from different interband transitions in comparison with the experiment [35].

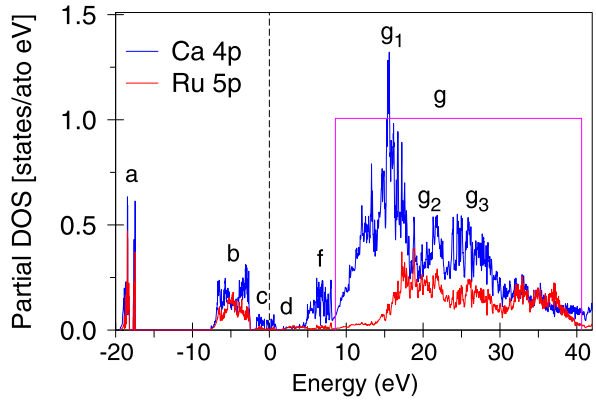

FIG. 12. The partial Ca $4p$ and Ru $5p$ DOS [in states/(atom eV)] in $Ca_3Ru_2O_7$ calculated in the GGA + SO + U ($U_{eff} = 1.3$ eV) approach.

dependence on the core level width: the larger Γ_{core}, the wider the XAS spectrum without a shape change (see the upper panel of Fig. 8). The RIXS spectra show nonlinear dependence on Γ_{core}, which strongly affects the spectrum shape.

Experimental measurements of the XAS, XMCD, and RIXS spectra at the Ca L_3, M_3, and Ru M_3 edges are highly desirable.

C. O, Ca, and Ru K RIXS spectra

The RIXS spectra at the O K edge in $Ca_3Ru_2O_7$ were measured by Arx *et al.* [35] up to 5 eV. The O K RIXS spectrum consists of a peak centered at zero energy loss, which includes the elastic line and other low energy features such as phonons and magnons, two inelastic excitations at 0.5 and 1.8 eV, and a major peak at ~3.3 (Fig. 11). We found that the first two low energy features are due to interband transitions between occupied and empty $O_{t_{2g}}$ states, which appear as a result of the strong hybridization between oxygen $2p$ states with Ru t_{2g} LEB and UEB in the vicinity of the Fermi level (see Fig. 3). Therefore, the oxygen K RIXS spectroscopy can be used for the estimation of the energy band gap and positions of Ru $4d$ Hubbard bands. The major peak at 3.3 eV reflects interband transitions from occupied O $2p$ states to the empty oxygen states which originate from the hybridization with Ru t_{2g} states. We found that the theory reproduces well the shape and energy position of the two low energy features. The energy position of the major peak at 3.3 eV is also reproduced well by theory, although our calculations give a wider major peak in comparison with the experiment. The interband transitions $O_{2p} \rightarrow O_{e_g}$ are relatively small and occupy a wide energy interval from 4.1 to 11 eV.

Let us consider now the XAS, XMCD, and RIXS spectra at the Ru and Ca K edges. For that, we first present the partial Ca $4p$ and Ru $5p$ DOS in Fig. 12 in a wide energy interval from −20 to 40 eV. We distinguish several groups of the bands. Group a derives from the hybridizations of the p states with corresponding Ca $4s$ and Ru $5s$ states. Group b is due to the hybridization with oxygen $2p$ states. Groups c and d are from the hybridization with Ru t_{2g} LEB and UEB, respectively. The group f comes from the hybridization with Ru e_g states. At last, the very wide structure g, which we divide into several subgroups, is the Ca $4p$ and Ru $5p$ bands themselves.

Figure 13 presents the theoretically calculated XAS (the upper panel) and XMCD (the lower panel) at the Ca and Ru K edges. The four fine structures f, g_1, g_2, and g_3 in the Ca K XAS spectrum can be easily distinguished as transitions from the Ca $1s$ core level into corresponding groups of the Ca $4p$ states with the same labels. The width of the Ru $1s$ core level is much larger than the Ca one ($\Gamma_{1s}^{Ru} = 5.33$ eV and $\Gamma_{1s}^{Ca} = 0.77$ eV [52]); therefore, the Ru K XAS spectrum possesses less structured features. The XMCD spectra at both

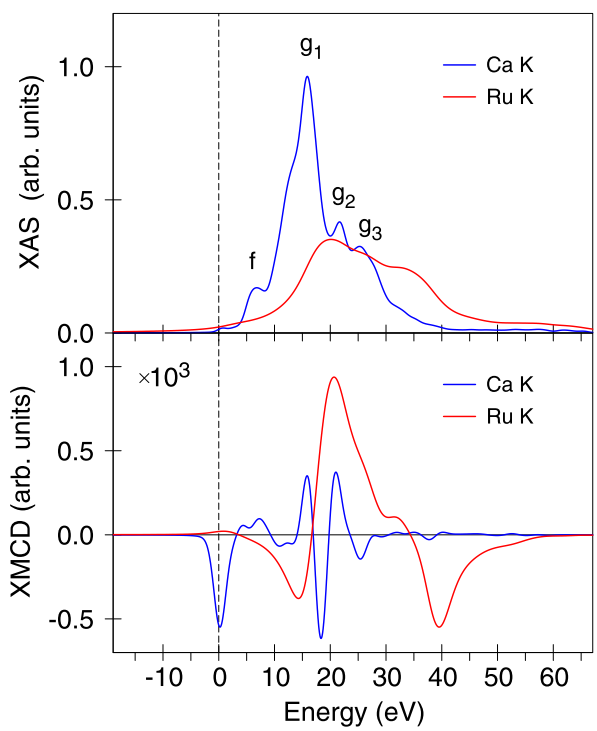

FIG. 13. The theoretically calculated XAS (the upper panel) and XMCD spectra (the lower panel) at the Ca and Ru K edges in $Ca_3Ru_2O_7$ calculated in the GGA + SO + U approach ($U_{eff} = 1.3$ eV).

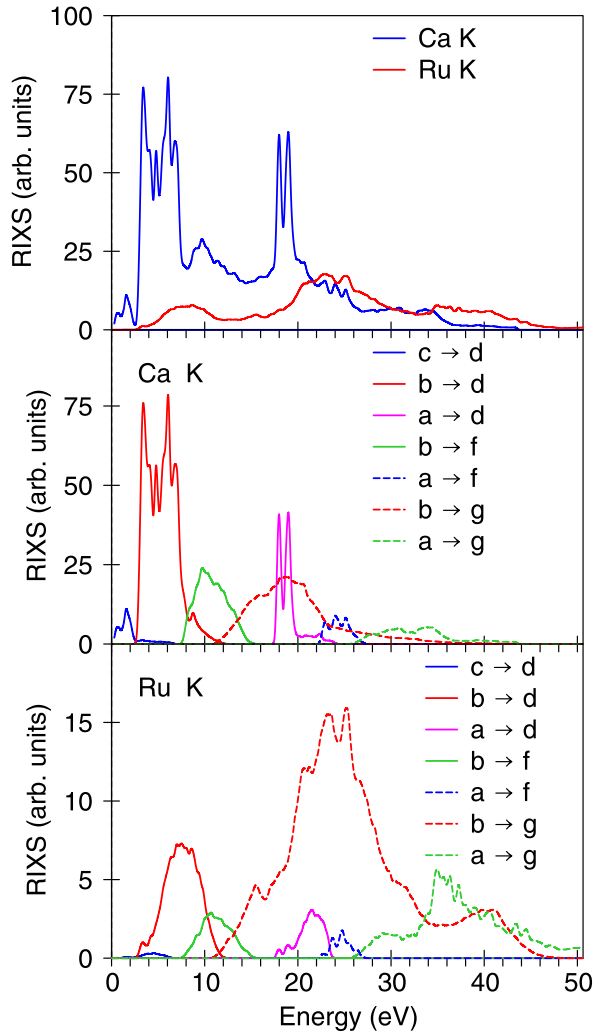

FIG. 14. The theoretically calculated RIXS spectra at the Ca and Ru K edges (the upper panel) and partial contributions to the RIXS spectra from different interband transitions (the lower panel) in $Ca_3Ru_2O_7$ calculated in the GGA + SO + U approach (U_{eff} = 1.3 eV).

Ca and Ru K edges are at least 3 orders of magnitude smaller than the corresponding XAS spectra.

Figure 14 (the upper panel) presents the theoretically calculated Ca and Ru K RIXS spectra in $Ca_3Ru_2O_7$. The spectra significantly differ from each other. The partial contributions from different interband transitions are also presented in Fig. 14 at the Ru (the lower panel) and Ca (the middle panel) K edges. The $c \rightarrow d$ ($t_{2g} \rightarrow t_{2g}$) transitions are visible at the Ca site, but they are quite small at the Ru one. The transitions to empty t_{2g} UEB states from the p states which are hybridized with corresponding oxygen $2p$ and $2s$ states ($b \rightarrow d$ and $a \rightarrow d$, respectively) are quite sharp and intense at the Ca site and suppressed at the Ru one due to the very large width of the Ru $1s$ core level. The largest contribution to the Ru K RIXS spectrum comes from $b \rightarrow g$ transitions. They are also shifted toward higher energy in comparison with the Ca K spectrum due to the corresponding shift of empty Ru $5p$ states with respect to Ca $4p$ states (see Fig. 12).

Experimental measurements of the XAS, XMCD, and RIXS spectra at the Ca and Ru K edges are also highly desirable.

V. CONCLUSIONS

Our calculations show that $Ca_3Ru_2O_7$ has a novel Mott insulating state, which is induced by the interplay of SO coupling and Coulomb repulsion.

The electronic and magnetic properties of $Ca_3Ru_2O_7$ oxide have been investigated theoretically using first-principle calculations in the frame of the fully relativistic spin-polarized Dirac LMTO band structure method to understand the importance of Coulomb interaction and SOC. The GGA approximation produces a metallic ground state in $Ca_3Ru_2O_7$ in contradiction to experimental data which show that this oxide is a Mott-like AFM insulator. To produce the correct ground state, one has to take into account strong Coulomb correlations. The GGA + SO + U approach shifts the occupied and empty t_{2g} bands downward and upward, respectively, by $U_{eff}/2$ producing a dielectric ground state in $Ca_3Ru_2O_7$ with a direct energy gap of 0.215 eV and an indirect one of 0.053 eV. The energy gap is increased with increasing Hubbard U. We found that in the ground state, $Ca_3Ru_2O_7$ possesses an AFM-b magnetic structure with the Ru spin moments ordered antiferromagnetically along the b axis, which is consistent with experimental data. The Ru spin and orbital moments are parallel in $Ca_3Ru_2O_7$ in accordance with Hund's third rule. The spin and orbital parts of the magnetic moments for the Ca ions in $Ca_3Ru_2O_7$ are found to be quite small. The magnetic moments at the oxygen sites are also relatively small, with the largest spin moments at the O_4 site and the smallest ones at the O_2 site.

We have theoretically investigated the XAS, XMCD, and RIXS spectra at the Ru and Ca L_3, M_3, and K edges as well as at the O K edge of the $Ca_3Ru_2O_7$ oxide. The calculated results are in good agreement with available experimental data. We have found that the best agreement between the theory and experiment in the RIXS spectra at the Ru L_3 edge can be achieved for U_{eff} = 1.3 eV. The calculations with larger values of U_{eff} shift the RIXS spectrum toward higher energies.

The experimentally measured RIXS spectrum of $Ca_3Ru_2O_7$ at the Ru L_3 edge possesses a sharp feature below 2 eV corresponding to transitions within Ru t_{2g} levels. The excitation located from 2 to 4 eV is due to $t_{2g} \rightarrow e_g$ transitions. The third wide structure situated at 4.5–11 eV appears due to transitions between Ru $4d_O$ states and e_g and t_{2g} states. The RIXS spectra at the L_3 and M_3 edges have to possess similar shapes because they reflect similar interband transitions. This is true indeed in the case of the Ru L_3 and M_3 RIXS spectra. However, the shapes of the L_3 and M_3 RIXS spectra at the Ca site quite differ from each other. Such a puzzle can be explained by the difference in the widths of corresponding core levels. The significantly larger width of the $3p_{3/2}$ core level leads to the suppression of the low energy fine structures in the Ca M_3 RIXS spectrum.

The RIXS spectrum at the O K edge consists of three major inelastic excitations. We found that the two low energy features $\leqslant$2.5 eV are due to interband transitions between occupied and empty $O_{t_{2g}}$ states which appear due to the strong

hybridization between oxygen $2p$ and Ru t_{2g} states in close vicinity to the Fermi level. The next major peak at 2.5–8 eV reflects interband transitions between occupied O $2p$ and empty oxygen states which originate from the hybridization with Ru t_{2g} states. Rather weak $O_{2p} \rightarrow O_{e_g}$ transitions occupy a wide energy interval between 4 and 11 eV. Although the partial Ca $4p$ and Ru $5p$ densities of states possess similar energy band structures, the RIXS spectra at the Ca and Ru K edges significantly differ from each other due to the difference in the widths of corresponding $1s$ core levels.

ACKNOWLEDGMENT

We are grateful to Dr. Alexander Yaresko from the Max Planck Institute FKF in Stuttgart for helpful discussions.

[1] Y. Maeno, H. Hashimoto, K. Yoshida, S. Nishizaki, T. Fujita, J. G. Bednorz, and F. Lichtenberg, Nature (London) **372**, 532 (1994).

[2] Y. Maeno, T. M. Rice, and M. Sigrist, Phys. Today **54**(1), 42 (2001).

[3] G. Cao, S. McCall, M. Shepard, J. E. Crow, and R. P. Guertin, Phys. Rev. B **56**, 321 (1997).

[4] L. Klein, L. Antognazza, T. H. Geballe, M. R. Beasley, and A. Kapitulnik, Phys. Rev. B **60**, 1448 (1999).

[5] H. Shaked, J. D. Jorgensen, O. Chmaissem, S. Ikeda, and Y. Maeno, J. Solid State Chem. **154**, 361 (2000).

[6] G. Cao, K. Abbound, S. McCall, J. E. Crow, and R. P. Guertin, Phys. Rev. B **62**, 998 (2000).

[7] Y. Yoshida, S. I. Ikeda, H. Matsuhata, N. Shirakawa, C. H. Lee, and S. Katano, Phys. Rev. B **72**, 054412 (2005).

[8] R. A. Borzi, S. A. Grigera, J. Farrell, R. S. Perry, S. J. S. Lister, S. L. Lee, D. A. Tennant, Y. Maeno, and A. P. Mackenzie, Science **315**, 214 (2007).

[9] S. I. Ikeda, Y. Maeno, S. Nakatsuji, M. Kosaka, and Y. Uwatoko, Phys. Rev. B **62**, R6089 (2000).

[10] G. Cao, S. McCall, J. E. Crow, and R. P. Guertin, Phys. Rev. Lett. **78**, 1751 (1997).

[11] X. Ke, T. Hong, J. Peng, S. E. Nagler, G. E. Granroth, M. D. Lumsden, and Z. Q. Mao, Phys. Rev. B **84**, 014422 (2011).

[12] E. Ohmichi, Y. Yoshida, S. I. Ikeda, N. Shirakawa, and T. Osada, Phys. Rev. B **70**, 104414 (2004).

[13] Y. Yoshida, I. Nagai, S. I. Ikeda, N. Shirakawa, M. Kosaka, and N. Mori, Phys. Rev. B **69**, 220411 (2004).

[14] C. D. Dashwood, L. S. I. Veiga, Q. Faure, J. G. Vale, D. G. Porter, S. P. Collins, P. Manuel, D. D. Khalyavin, F. Orlandi, R. S. Perry, R. D. Johnson, and D. F. McMorrow, Phys. Rev. B **102**, 180410(R) (2020).

[15] W. Bao, Z. Q. Mao, Z. Qu, and J. W. Lynn, Phys. Rev. Lett. **100**, 247203 (2008).

[16] D. A. Sokolov, N. Kikugawa, T. Helm, H. Borrmann, U. Burkhardt, R. Cubitt, J. S. White, E. Ressouche, M. Bleuel, K. Kummer, A. P. Mackenzie, and U. K. Robler, Nat. Phys. **15**, 671 (2019).

[17] S. McCall, G. Cao, J. E. Crow, N. Harrison, C. H. Mielke, A. H. Lacerda, and R. P. Guertin, Phys. B: Condens. Matter **246-247**, 144 (1998).

[18] G. Cao, L. Balicas, Y. Xin, E. Dagotto, J. E. Crow, C. S. Nelson, and D. F. Agterberg, Phys. Rev. B **67**, 060406(R) (2003).

[19] G. Cao, X. N. Lin, L. Balicas, S. Chikara, J. E. Crow, and P. Schlottmann, New J. Phys. **6**, 159 (2004).

[20] A. V. Puchkov, M. C. Schabel, D. N. Basov, T. Startseva, G. Cao, T. Timusk, and Z.-X. Shen, Phys. Rev. Lett. **81**, 2747 (1998).

[21] G. Cao, S. C. McCall, J. E. Crow, and R. P. Guertin, Phys. Rev. B **56**, 5387 (1997).

[22] J. S. Lee, S. J. Moon, B. J. Yang, J. Yu, U. Schade, Y. Yoshida, S.-I. Ikeda, and T. W. Noh, Phys. Rev. Lett. **98**, 097403 (2007).

[23] H. L. Liu, S. Yoon, S. L. Cooper, G. Cao, and J. E. Crow, Phys. Rev. B **60**, R6980 (1999).

[24] I. I. Mazin and D. J. Singh, Phys. Rev. B **56**, 2556 (1997).

[25] T. Mizokawa, L. H. Tjeng, G. A. Sawatzky, G. Ghiringhelli, O. Tjernberg, N. B. Brookes, H. Fukazawa, S. Nakatsuji, and Y. Maeno, Phys. Rev. Lett. **87**, 077202 (2001).

[26] Z. Fang, N. Nagaosa, and K. Terakura, Phys. Rev. B **69**, 045116 (2004).

[27] G.-Q. Liu, V. N. Antonov, O. Jepsen, and O. K. Andersen, Phys. Rev. Lett. **101**, 026408 (2008).

[28] M. W. Haverkort, I. S. Elfimov, L. H. Tjeng, G. A. Sawatzky, and A. Damascelli, Phys. Rev. Lett. **101**, 026406 (2008).

[29] J. Bertinshaw, M. Krautloher, H. Suzuki, H. Takahashi, A. Ivanov, H. Yavas, B. J. Kim, H. Gretarsson, and B. Keimer, Phys. Rev. B **103**, 085108 (2021).

[30] D. J. Singh and S. Auluck, Phys. Rev. Lett. **96**, 097203 (2006).

[31] G.-Q. Liu, Phys. Rev. B **84**, 235137 (2011).

[32] Z. Jin and W. Ku, arXiv:1809.04589.

[33] I. Marković, M. D. Watson, O. J. Clark, F. Mazzola, E. A. Morales, C. A. Hooley, H. Rosner, C. M. Polley, T. Balasubramanian, S. Mukherjee, N. Kikugawa, D. A. Sokolov, A. P. Mackenzie, and P. D. C. King, Proc. Natl. Acad. Sci. **117**, 15524 (2020).

[34] D. Puggioni, M. Horio, J. Chang, and J. M. Rondinelli, Phys. Rev. Res. **2**, 023141 (2020).

[35] K. von Arx, F. Forte, M. Horio, V. Granata, Q. Wang, L. Das, Y. Sassa, R. Fittipaldi, C. G. Fatuzzo, O. Ivashko, Y. Tseng, E. Paris, A. Vecchione, T. Schmitt, M. Cuoco, and J. Chang, Phys. Rev. B **102**, 235104 (2020).

[36] L. J. P. Ament, M. van Veenendaal, T. P. Devereaux, J. P. Hill, and J. van den Brink, Rev. Mod. Phys. **83**, 705 (2011).

[37] V. V. Nemoshkalenko, A. E. Krasovskii, V. N. Antonov, V. N. Antonov, U. Fleck, H. Wonn, and P. Ziesche, Phys. Status Solidi B **120**, 283 (1983).

[38] E. Arola, P. Strange, and B. L. Gyorffy, Phys. Rev. B **55**, 472 (1997).

[39] V. N. Antonov, D. A. Kukusta, and L. V. Bekenov, Phys. Rev. B **105**, 155144 (2022).

[40] G. Y. Guo, H. Ebert, W. M. Temmerman, and P. J. Durham, Phys. Rev. B **50**, 3861 (1994).

[41] V. Antonov, B. Harmon, and A. Yaresko, *Electronic Structure and Magneto-Optical Properties of Solids* (Kluwer, Dordrecht, 2004).

[42] E. Arola, M. Horne, P. Strange, H. Winter, Z. Szotek, and W. M. Temmerman, Phys. Rev. B **70**, 235127 (2004).
[43] V. N. Antonov, O. Jepsen, A. N. Yaresko, and A. P. Shpak, J. Appl. Phys. **100**, 043711 (2006).
[44] V. N. Antonov, B. N. Harmon, A. N. Yaresko, and A. P. Shpak, Phys. Rev. B **75**, 184422 (2007).
[45] V. N. Antonov, A. N. Yaresko, and O. Jepsen, Phys. Rev. B **81**, 075209 (2010).
[46] O. K. Andersen, Phys. Rev. B **12**, 3060 (1975).
[47] J. P. Perdew, K. Burke, and M. Ernzerhof, Phys. Rev. Lett. **77**, 3865 (1996).
[48] P. E. Blöchl, O. Jepsen, and O. K. Andersen, Phys. Rev. B **49**, 16223 (1994).
[49] A. N. Yaresko, V. N. Antonov, and P. Fulde, Phys. Rev. B **67**, 155103 (2003).
[50] P. H. Dederichs, S. Blügel, R. Zeller, and H. Akai, Phys. Rev. Lett. **53**, 2512 (1984).
[51] W. E. Pickett, S. C. Erwin, and E. C. Ethridge, Phys. Rev. B **58**, 1201 (1998).
[52] J. L. Campbell and T. Parr, At. Data Nucl. Data Tables **77**, 1 (2001).
[53] J. Kim, M. Daghofer, A. H. Said, T. Gog, J. van den Brink, G. Khaliullin, and B. J. Kim, Nat. Commun. **5**, 4453 (2014).
[54] J. Nichols, N. Bray-Ali, A. Ansary, G. Cao, and K.-W. Ng, Phys. Rev. B **89**, 085125 (2014).
[55] J.-K. Kim, C. Dietl, H.-W. J. Kim, S.-H. Ha, J. Kim, A. H. Said, J. Kim, and B. J. Kim, J. Synchrotron Rad. **30**, 643 (2023).
[56] V. N. Antonov, D. A. Kukusta, and L. V. Bekenov, Phys. Rev. B **109**, 165120 (2024).